ACS APPLIED MATERIALS & INTERFACES

Research Article

www.acsami.org

Binary Nickel–Cobalt Oxides Electrode Materials for High-Performance Supercapacitors: Influence of its Composition and Porous Nature

J. Zhang, F. Liu, J. P. Cheng,* and X. B. Zhang

State Key Laboratory of Silicon Materials, School of Materials Science & Engineering, Key Laboratory of Advanced Materials and Applications for Batteries of Zhejiang Province, Zhejiang University, Hangzhou 310027, P.R. China

Ⓢ *Supporting Information*

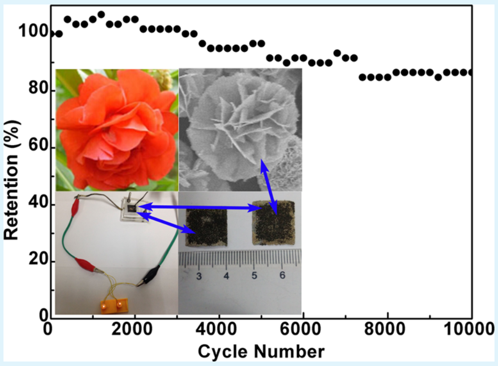

ABSTRACT: Nickel–cobalt oxides were prepared by coprecipitation of their hydroxides precursors and a following thermal treatment under a moderate temperature. The preformed nickel-cobalt bimetallic hydroxide exhibited a flower-like morphology with single crystalline nature and composed of many interconnected nanosheets. The ratio of Ni to Co in the oxides could easily be controlled by adjusting the composition of the original reactants for the preparation of hydroxide precursors. It was found that both the molecular ratio of Ni to Co and the annealing temperature had significant effects on their porous structure and electrochemical properties. The effect of the Ni/Co ratio on the pseudocapacitive properties of the binary oxide was investigated in this work. The binary metal oxide with the exact molar ratio of Ni:Co = 0.8:1 annealed at 300 °C, showing an optimum specific capacitance of 750 F/g. However, too high an annealing temperature would lead to a large crystal size, a low specific surface area, as well as a much lower pore volume. With the use of the binary metal oxide with Ni:Co = 0.8:1 and activated carbon as the positive and negative electrode, respectively, the assembled hybrid capacitor could exhibit a high-energy density of 34.9 Wh/kg at the power density of 875 W/kg and long cycling life (86.4% retention of the initial value after 10000 cycles).

KEYWORDS: *nickel-cobalt oxides, pseudocapacitive property, hybrid capacitor, porous structure, hydrothermal*

1. INTRODUCTION

Developing a supercapacitor (SC) with a high capacitance is of great importance for the newly designed power delivery systems because of the low-energy densities of conventional capacitors (0.01–0.05 Wh/kg). The RuO_2 had been considered as a promising electrode material, owing to its high theoretical specific capacitance; however, it is rather expensive and toxic and not suitable for a wide commercialization and application. Thus, other conventional and inexpensive transition metal oxides or hydroxides have been intensively investigated with the target to achieve a high specific capacitance, good rate capability, and long cycle life.[1−3] Generally, transition metal hydroxide is of a low conductivity and is hard to deliver a high performance under high-rate current densities.[4,5] By contrast, transition metal oxides are semiconductive with a higher electrical conductivity and have been intensively investigated as electrode materials.

Among various transition metal oxides, NiO has been considered as one of the most promising electrode materials for SC due to its satisfactory performance, low cost, and natural abundance.[6,7] However, there are still some drawbacks for it, such as low electrical conductivity and poor reversibility. In order to further improve the capacitive performance of NiO, reducing its particle size and forming a three-dimensional (3D) porous architecture are two common choices. In addition, coupling NiO with different electrode materials (e.g., other transition metal oxides[8−12] and carbon-based materials[13]) has also been extensively investigated. In this way, NiO was prepared as a guest material by an additional process. M. C. Liu et al. developed the nickel/cobaltite oxide composite ($NiO/NiCo_2O_4/Co_3O_4$) for SC electrode material with a specific capacitance of 1717 F/g at the current density of 5 mA/cm^2.[11] J. P. Liu and co-workers synthesized MnO_2–NiO nanoflake-assembled tubular arrays on stainless steel which exhibited a good rate performance and long cycle life,[8] for both MnO_2 and NiO could contribute to charge storage simultaneously.

To date, significant efforts have been made to improve the electrochemical performance of the electrode materials by coupling different electroactive materials. Mixed transition metal oxides have thus received a lot of attention due to their multiple oxidation, high energy density, and high specific capacitance.[14−26] Especially, if two transition metals are coincorporated into the host layer, better capacity and cycling stability are possibly achieved in comparison with monometallic

Received: February 4, 2015
Accepted: July 23, 2015
Published: July 23, 2015

ACS Publications

DOI: 10.1021/acsami.5b04463
ACS Appl. Mater. Interfaces 2015, 7, 17630−17640

systems.[27−29] Meanwhile, to achieve a high energy density for SCs, the electrode materials should possess sufficient surface electroactive species and facilitate the transition of electrons for Faradaic redox reactions. Therefore, a 3D integrated hierarchical structure and porous features are preferred for electrode materials.[30−33] Concerning all above issues, mixed metal oxides containing nickel and cobalt are worthy of being developed and investigated due to the possible synergistic effects occurring between them.[34−37] Co-based oxide has long been considered as a promising electrode material for its specific structure and excellent pseudocapacitive properties too. Previous experimental results indicated that the incorporation of Co into NiO could enhance the reversibility and conductivity of NiO[38] and that the effects of Ni/Co molar ratio on the specific capacitance was very important.[35] Thus, binary Ni−Co oxides can exhibit higher electrical conductivity and improved electrochemical activity. Various Ni−Co oxide compounds have been synthesized by different methods, including sol−gel,[39,40] electrodeposition,[20,41] hydrothermal method,[27,42] and coprecipitation.[34,43,44] Among them, hydrothermal method is one of the best choices because of its easy controlling in crystal size, morphology, and structure, convenient manipulation as well as low synthesis temperature. Note that some chelating agents play an important role in the hydrothermal process. However, removal of them from the resultant product is difficult and time-consuming and needs extra treatment. Surfactant-free hydrothermal strategy in a pure water system is considered as a simple and robust choice then.

On the basis of above viewpoints, a facile two-step method is reported to prepare Ni−Co binary oxides to achieve a high specific capacitance for SC application. In our case, Ni−Co binary hydroxides with a 3D flower-like morphology are first synthesized by surfactant-free hydrothermal method with various Ni/Co molar ratios. Subsequently, they are annealed under a moderate temperature, and porous Ni−Co oxide compounds are then obtained. Our results prove that the total specific capacitance of the binary metal oxide is highly composition-dependent and that a precise composition control for the series of oxide is necessary. Moreover, the porous features of the oxides are also strongly related with their composition. Thus, a simple process for the preparation of Ni−Co binary oxides with high-performance is practically desirable. Pseudocapacitive performances of the Ni−Co binary oxides with different compositions are studied and compared with their individual oxides. Our method for the preparation of Ni−Co binary oxides is simple, controllable, and easy to realize the scale production.

2. EXPERIMENTAL SECTION

2.1. Preparation of Metal Oxides. Flower-like Ni−Co oxide microspheres were synthesized by a hydrothermal route with a following annealing treatment. In a typical process, 10 mmol metallic nitrate salts (the Ni/Co molar ratios were tuned to be 1:0, 7:3, 5:5, 3:7, and 0:1) and 15 mmol hexamethylenetetramine (HMT) were dissolved into 32 mL water under stirring. Then, the solution was transferred into a 100 mL Teflon-lined stainless-steel autoclave, and it was maintained in the oven at 120 °C for 2 h.[28] After cooling it down to room temperature, a green hydroxide precipitate was collected and washed with adequate water, and then dried in an oven at 80 °C. Finally, the hydroxides prepared with different Ni/Co molar ratios were annealed at 300 °C for 2 h in air to obtain black oxide samples. The sample prepared with initial Ni/Co molar ratio of 1:0, 7:3, 5:5, 3:7, and 0:1 is denoted as N1, C3N7, C5N5, C7N3, and C1, respectively. As a control, the hydroxide with Ni/Co of 3:7 was annealed at 500 °C for 2 h, and the resultant sample was named C7N3-500 here.

2.2. Material Characterization. The morphology and phase of the samples were characterized by a scanning electron microscope (SEM, Hitachi S-4800), a transmission electron microscope (TEM, Philips CM200), and a powder X-ray diffractometer (XRD, Shimadzu XRD-6000) with Cu Kα irradiation (λ = 1.5406 Å). Thermogravimetric analysis (TGA) was measured using a TA Q600 instrument from 25 to 600 °C with a heating rate of 10 °C/min in air. The elemental composition and oxidation state were analyzed using X-ray photoelectron spectroscopy (XPS, Thermo, Escalab 250xi). X-ray fluorescence spectrometer (XRF, ARL ADVANT'X IntelliPowerTM 4200, ThermoFisher) was used to determine the content of Ni−Co in the binary metal oxides. The specific surface areas and pore diameter distributions of the oxides were calculated at 77 K in N_2 by a Micromeritics ASAP 2020 (Micromeritics Instrument Corporation) analyzer with a method of Brunauer-Emmet-Teller (BET) and BJH (Barrett−Joyner−Halenda). Before gas-sorption measurement, each sample was degassed in vacuum at 300 °C for 10 h.

2.3. Electrochemical Measurements. The working electrode was prepared by coating the homogeneous slurry of metal oxide, acetylene black, and polyvinylidene fluoride in a weight ratio of 8:1:1 in *N*-methyl-2-pyrrolidone onto 1.5 × 1.5 cm Ni foam as the current collector. The electrode was then completely dried at 80 °C in vacuum. The electrode was pressed to be a thin foil at 10 MPa before each test. The mass of active material loaded on each electrode was about 5 mg by means of a microbalance (Sartorius, BS124S) with an accuracy of 0.1 mg. All electrochemical measurements were performed in 2 M KOH aqueous solution under a standard three-electrode system for electrode materials. The Ni foam loaded with active material, platinum foil, and Ag/AgCl electrode were used as a working electrode, counter electrode, and reference electrode, respectively. Cyclic voltammograms (CV), galvanostatic charge−discharge, and electrochemical impedance spectroscopy (EIS) were measured by a CHI660D electrochemical workstation. The cycle life measurement was tested on a LAND CT2001A test system by galvanostatic charge−discharge techniques.

To prepare a hybrid (asymmetric) SC, Ni−Co metal oxide (sample C7N3) and activated carbon (AC) were selected as positive and negative electrode materials, respectively, with a polypropylene membrance as a separator. The hybrid SC could work in a much wider potential window (c.a., 1.75 V). The mass on each electrode was balanced with a law of $Q_+ = Q_-$ ($Q = cm\Delta V$) to ensure an efficient charge storage,[28] where Q (C) is the storage charges of the electrode, C (F g^{-1}) is the specific capacitance of the electrode based on the mass of active material, m (g) is the mass of active material within the working electrode, and ΔV (V) is the potential window.

3. RESULTS AND DISCUSSION

3.1. Structure and Composition Analysis. The phases of the hydroxide precursors prepared with different Ni/Co ratios were first characterized by powder XRD. As shown in Figure 1a, all their diffraction peaks can be ascribed to hydrotalcite-like structures, such as α-Ni(OH)$_2$, α-Co(OH)$_2$, and Ni−Co layered double hydroxide. This phenomenon is attributed to the formation of Ni−Co binary hydroxide compounds. When the hydroxide precursors were heated at 300 °C for 2 h, they transformed to the corresponding fcc oxides, such as spinel Co_3O_4 (sample C1), $NiCo_2O_4$ (binary oxides), and cubic NiO (sample N1), as shown in Figure 1b. All these diffraction peaks can be well-indexed to a cubic Co_3O_4 (JCPDS: 43-1003), NiO (JCPDS: 47-1049), and $NiCo_2O_4$ (JCPDS: 73-1702). No other peaks from hydroxides can be observed. Thus, we believe the complete transition from hydroxides to oxides after annealing at 300 °C. However, the diffraction peaks of NiO (i.e., sample N1) are much broader than those of Co_3O_4 (sample C1), implying a much smaller crystal size of NiO than Co_3O_4. The

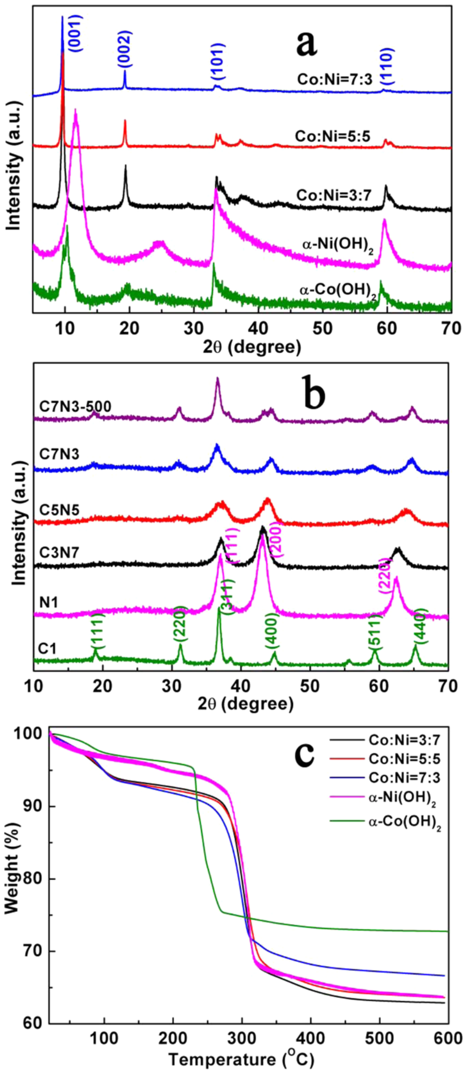

Figure 1. XRD patterns of (a) hydroxide precursors and (b) transition metal oxides. (c) TGA curves of hydroxides precursors.

average crystal sizes of the metal oxides are determined to be 10, 9, 11, 12, and 16 nm for sample N1, C3N7, C5N5, C7N3, and C1, respectively, which is calculated by the Scherrer equation.[21] The crystal size of sample C7N3-500 is calculated to be 13 nm, a little larger than that of sample C7N3 annealed at 300 °C.

The metal hydroxide precursor is not thermally stable. It decomposes on calcination and transforms into the corresponding metal oxide. TGA curves of the as-prepared hydroxide precursors with different Ni/Co ratios were measured in air between 25 and 600 °C to investigate their decomposition performance. As shown in Figure 1c, we can observe two significant weight loss steps from each curve. The first weight loss below 150 °C is likely due to the evaporation of physically absorbed water and trapped anions, while the second is assigned to the decomposition of hydroxide and the crystallization of metal oxide crystals. We can observe that the crystallization temperature for Co_3O_4, Ni−Co binary oxides, and NiO are at about 230, 270, and 280 °C, respectively, from their TGA curves. Above 400 °C, there is no evident weight loss for all samples, indicating a complete phase transition. Since the crystallization temperature of NiO is higher than that of Co_3O_4, we can deduce that the crystal size of NiO is much smaller than Co_3O_4 when being annealed at the same temperature, as also proved by XRD analysis.

The general morphologies and microstructure of the as-synthesized materials were observed by SEM and TEM, as displayed in Figure 2. Figure 2 (panels a−f) shows the typical SEM images of metal oxides, indicating a flower-like structure. Comparing with their hydroxide precursors (shown in Figure S1), no significant morphological changes of the metal oxides can be observed after annealing.[28] Figure 2f shows the SEM image of sample C7N3-500. Due to its large crystal size and high annealing temperature, a lot of small pores can be clearly seen on the surface, indicating its porous nature. The metal oxides derived from hydroxide precursors usually involve the recrystallization process and the release of gaseous species. It will create a highly porous texture or hollow structure and exhibit a high specific surface area, which benefits the performance in electrochemical applications with a short ionic/electronic diffusion length.[45]

TEM images of sample C7N3 and its hydroxide precursor are shown in Figure 2 (panels g−i). In Figure 2g, we can see that the hydroxide precursor is of a sheet-like structure with a homogeneous thickness. The corresponding electron diffraction (ED) pattern in the inset confirms that the normal of the nanosheets is the [001] direction of hydroxide from the hexagonal (110) diffraction spots and that they are single crystalline. After the heat treatment, it sustains the original morphology of its precursor, as shown in Figure 2h. However, the sheet-like oxide is composed of a large amount of small nanoparticles. Close observations indicate that there are a lot of small pores distributing in the metal oxide nanosheet, typically shown in Figure 2i. The size of nanoparticles in the nanosheet is about 10 nm within a narrow size distribution. They are closely connected with their adjacent grains. The phase of the metal oxide nanoparticles was also identified by selected area ED technique as the spinel form of $NiCo_2O_4$ in the inset of Figure 2i. The distinct diffraction spots indicate the crystalline of the $NiCo_2O_4$ nanosheets. The calculated interplanar spacings by the ED pattern are in good agreement with those of $NiCo_2O_4$, as marked in the diffraction pattern. We deduce that these $NiCo_2O_4$ nanocrystals tend to agglomerate to form frame configurations, showing an oriented attachment between adjacent nanocrystals.[46] Otherwise, the diffraction pattern will be multicrystalline.

We also determined the Ni/Co molar ratio of the as-synthesized Ni−Co oxides by XRF. The XRF results demonstrate that the molar ratios of Ni to Co for samples C3N7, C5N5, and C7N3 are 3.4, 1.6 and 0.8, respectively, which are not consistent with those of the original reactants. The EDS analysis of their hydroxide precursors are shown in Figure S2). The measured Ni/Co ratios are consistent with what was determined by XRF, as shown in Table 1. The content of cobalt in Ni−Co binary oxides is much lower than that in the original reactants, which is caused by the higher solubility constant of $Co(OH)_2$ (5.92×10^{-15}) than $Ni(OH)_2$ (5.48×10^{-16}).[28] The Ni/Co molar ratio of sample C7N3 is closer to that of $NiCo_2O_4$ than those of sample C3N7 and C5N5. It means that there are much more $NiCo_2O_4$ crystals in sample C7N3 than in other two binary oxides. Due to the better electrochemical performance of binary metal oxide than monometallic oxide, we hypothesize that the binary oxides are composed of $NiCo_2O_4$ and NiO with different contents. In accordance with the measured molar ratio of Ni to Co, the mass contents of $NiCo_2O_4$ and NiO in the binary oxides are

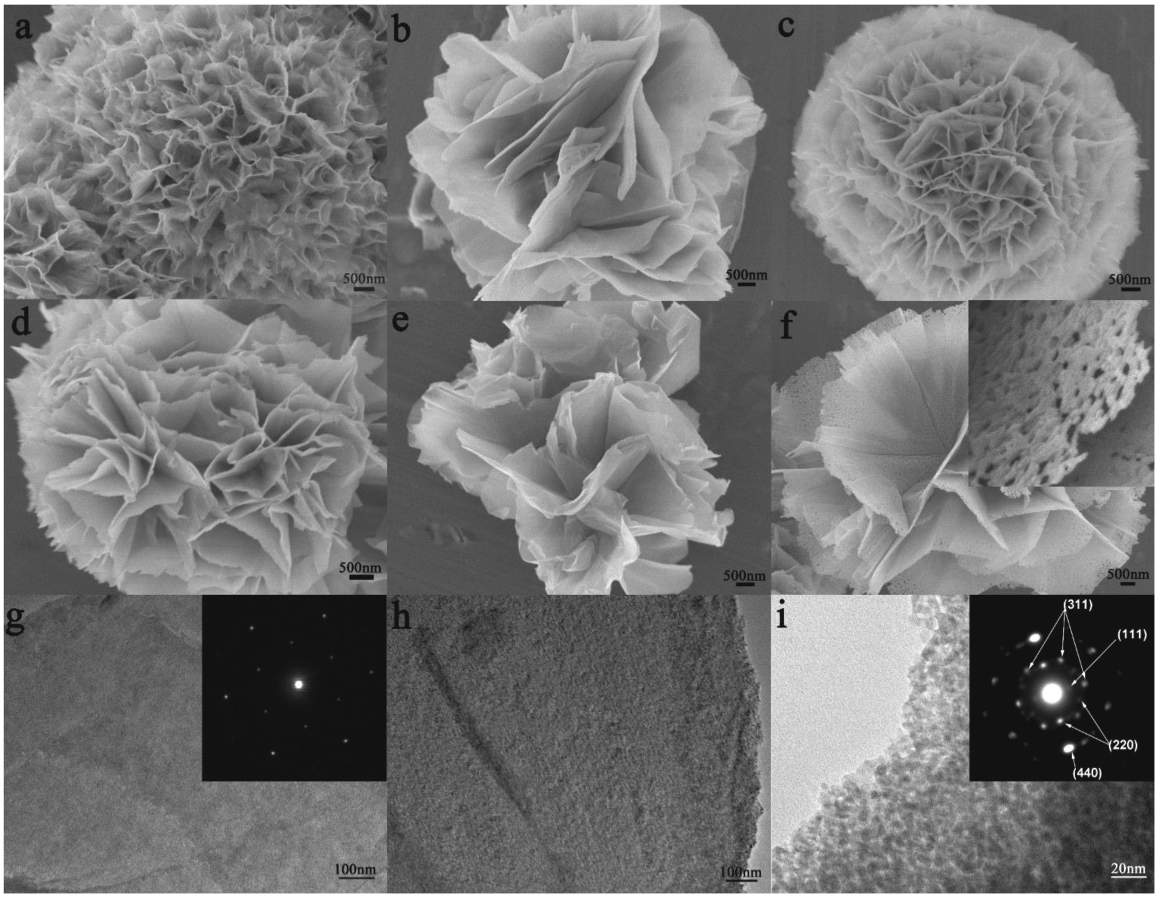

Figure 2. SEM images of as-prepared oxides (a) N1, (b) C1, (c) C3N7, (d) C5N5, (e) C7N3, and (f) C7N3-500; TEM images of (g) hydroxide precursor of sample C7N3, (h) and (i) sample C7N3 under different magnifications, with the inset of (i) showing the corresponding selected area ED pattern of sample C7N3.

Table 1. Measured Molar Ratio of Binary Hydroxides and Oxides and the Mass Contents of $NiCo_2O_4$ and NiO in the Ni−Co Binary oxides

metal oxide	molar ratio of Ni:Co in the hydroxide precursor by EDS	molar ratio of Ni:Co in binary oxide by XRF	mass content of $NiCo_2O_4$ (wt %)	mass content of NiO (wt %)
C3N7	3.1:1	3.4:1	36	64
C5N5	1.6:1	1.6:1	59	41
C7N3	0.8:1	0.8:1	84	16

calculated and demonstrated in Table 1. For samples C3N7 and C5N5, the high content of NiO in their compositions leads to a close similarity to sample N1 (pure NiO) in the XRD patterns.

The more detailed chemical composition and the elemental oxidation state of sample C7N3 are further characterized by the XPS measurement. The results are presented in Figure S4), indicating the presence of Ni, Co, and O (in Figure S4a). By using the Gaussian fitting method, the Ni 2p is well-fitted with two spin−orbit doublets, characteristic of Ni^{2+} and Ni^{3+} with two satellites (in Figure S4b). The fitting peaks at 853.7 and 871.2 eV are indexed to Ni^{2+}, while the peaks at 855.6 and 872.8 eV can be indexed to Ni^{3+}.[47] The satellite peaks at 860.7 and 878.8 eV are shakeup type peaks of nickel, at the high side of the Ni $2p_{1/2}$ and Ni $2p_{3/2}$.[48] The Co 2p emission spectrum (in Figure S4c) is also fitted with two spin−orbit doublets, characteristic of Co^{2+} and Co^{3+}. The peaks at binding energies of 779.3 and 794.2 eV are ascribed to Co^{3+}. The other two peaks at 781.3 and 795.9 eV can be ascribed to Co^{2+}.[47] The spectrum for the O 1s region (in Figure S4d) shows three oxygen contributions, which have been denoted as O1, O2, and O3, respectively. The fitting peak of O1 at 528.9 eV is a typical metal−oxygen bond, and that of O2 at 530.4 eV corresponds to a high number of defect sites with a low oxygen coordination in materials with a small particle size. The component O3 at 532.6 eV can be ascribed to a multiplicity of physically and chemically bonded water on or near the surface.[49] These results show that Ni−Co binary oxides have a mixed composition, containing Ni^{2+}, Ni^{3+}, Co^{2+}, and Co^{3+}, which are in good agreement with the results reported for $NiCo_2O_4$ in the literature.[47−49]

3.2. BET and Pore Volume Measurement. To investigate the specific surface area and the pore size distribution of the metal oxide microflowers, nitrogen gas-sorption measurement was performed for each sample. The nitrogen adsorption−desorption isotherms and the pore size distribution plots of the metal oxide samples are typically shown in Figure 3 and Figure S5. All the curves of metal oxide samples display H3-type sorption isotherms, with hysteresis loops characteristic of mesoporous materials. The adsorption isotherm in the low-relative-pressure region is attributed to the surface area of the microflowers, whereas the large hysteresis loops are due to the mesopores inside the microflowers.

The specific surface area and pore volume of the metal oxides are summarized in Table 2. We can find that the specific surface area of transition metal oxide is related to its composition. A high content of nickel in the hydroxide precursor results in a

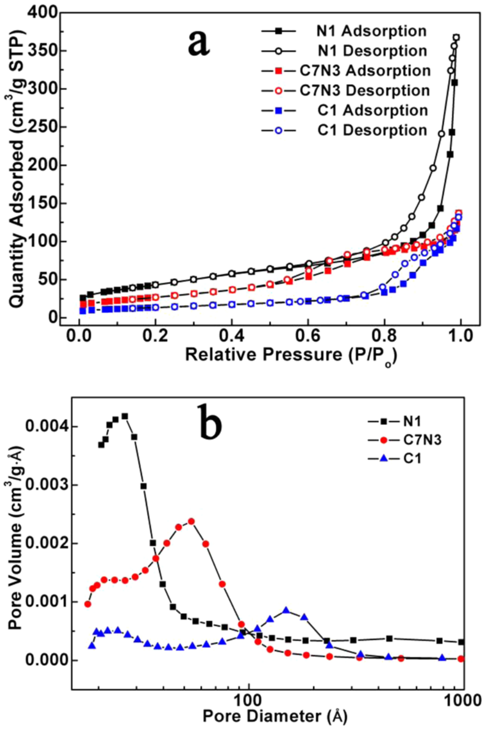

Figure 3. (a) Nitrogen adsorption−desorption isotherms and (b) BJH pore size distributions of metal oxide samples.

Table 2. Specific Surface Area and Pore Volume of Transition Metal Oxides

metal oxide	specific surface area (m^2/g)	pore volume (cm^3/g)	mesopore volume (cm^3/g)	mesopore/ total pore ratio (%)	annealing temperature (°C)
C1	47.74	0.2054	0.1503	73.2	300
C7N3	98.91	0.2166	0.1695	78.3	300
C5N5	121.90	0.2113	0.1761	83.3	300
C3N7	124.67	0.3120	0.1791	57.4	300
N1	156.94	0.5796	0.3227	55.7	300
C7N3-500	23.84	0.1213	0.0612	50.5	500

large specific area of the corresponding metal oxide under the same annealing temperature. This can be assigned to the small crystal size of NiO and the high decomposition temperature of nickel hydroxide, being in good agreement with the above XRD, SEM, and TEM observations. Under the same calcination temperature, the large Co_3O_4 nanoparticles recrystallize together and the pore size increase, so the hysteresis loop shifts to the right, as shown in Figure 3a. It is also consistent with the pore size distribution in Figure 3b. In addition to chemical composition, anealling temperature is also a key factor for controlling the porous structure and particle sizes of the metal oxide product. Similarly, when the Ni−Co hydroxide was heated at 500 °C, its specific surface area was greatly reduced to 1/4 of that heated at 300 °C. From Figure 3b and Table 2, it is obvious that the metal oxide with a small crystal size usually has a larger pore volume.

In the present work, we found that the Ni and Co composition in the flower-like microspheres can be readily manipulated by varying their concentrations in the chemical solution. This provides us an opportunity to control their composition, porous structure, and supercapacitive properties. In addition to NiO and Co_3O_4, nickel cobaltite ($NiCo_2O_4$) is also a low-cost, environmentally friendly transition metal oxide. They are widely reported to be potential electrode materials for SCs. $NiCo_2O_4$ is regarded as a mixed metal oxide consisting of a spinel type crystal structure, similar to Co_3O_4, where the nickel cations occupy octahedral sites and cobalt cations are distributed over the tetrahedral and octahedral sites randomly. However, the electronic conductivity of $NiCo_2O_4$ has been reported to be much higher than those of NiO and Co_3O_4. It has two orders higher electron conductivity compared with pure NiO or Co_3O_4 (10^{-3} to 10^{-2} S/cm) together with a high electrochemical activity.[50] It is documented to have 62 S/cm for single crystal $NiCo_2O_4$ nanoplate at room temperature[51] and 0.6 S/cm for the polycrystalline $NiCo_2O_4$ film.[14] Generally, $NiCo_2O_4$ can be directly prepared via one-pot approaches or transformed from some precursors such as hydroxides, carbonates, and organic materials. For our hydroxide precursors, the subsequent phase transition is accompanied by the release of nontoxic gases, and the product has a porous 3D hierarchical structure. Thus, we will focus on the electrochemical properties of the series of metal oxides containing Ni and Co in the following section.

It is believed that the redox reactions offered by $NiCo_2O_4$, including contributions from both the nickel and cobalt ions, are richer than those of the monometallic nickel oxide and cobalt oxide.[52,53] Previous reports are mainly focused on the $NiCo_2O_4$-carbon-based composite, porous $NiCo_2O_4$ with various morphologies, and its films on conducting substrate. Recently, some literature have utilized $NiCo_2O_4$ material as both active material and conductive backbone to support guest metal oxides, hydroxides or sulfides, so as to produce hierarchical mesopores with a large specific surface area.[52] To realize the above purpose, complex processes and additional fabrication are usually necessary. In our case, $NiCo_2O_4$ and NiO nanocrystals are homogeneously mixed and combined together to form a 3D hierarchical structure by a simple step. For the porous $NiCo_2O_4$ prepared by pyrolysis method, the product prepared at a low temperature usually exhibits a larger BET surface area and higher specific capacitance than that prepared at a high temperature.[54] Annealing temperature can be thus efficiently applied to control the surface area, pore volume, and electrochemical performance of the product.[55] In this work, porous $NiCo_2O_4$ with NiO can be fabricated by pyrolyzing the hydroxide precursors with different compositions. The binary hydroxide samples are calcined at the same temperature. After calcination, the specific surface area, pore volume, and electrochemical performance of the oxide samples are strongly related with their composition due to the different pyrolyzing temperatures of $Ni(OH)_2$ and $Co(OH)_2$.

3.3. Electrochemical Properties. The CV curves of transition metal oxides and nickel foam recorded at a scan rate of 5 mV/s in the potential range of 0−0.6 V are shown in Figure 4a. It can be clearly seen that the redox peaks of Ni foam are negligible in comparison with those of as-prepared metal oxides. Thus, we believe that these redox peaks are essentially attributed to electrode materials. As can be seen, the CV curves of metal oxides exhibit two pairs of strong redox peaks, indicating typical pseudocapacitor behavior. The two redox peaks can be attributed to the electrochemical reactions of Ni/Co species based on the following equations:

$$NiO + OH^- = NiOOH + e^- \quad (1)$$

$$Co_3O_4 + H_2O + OH^- = 3CoOOH + e^- \quad (2)$$

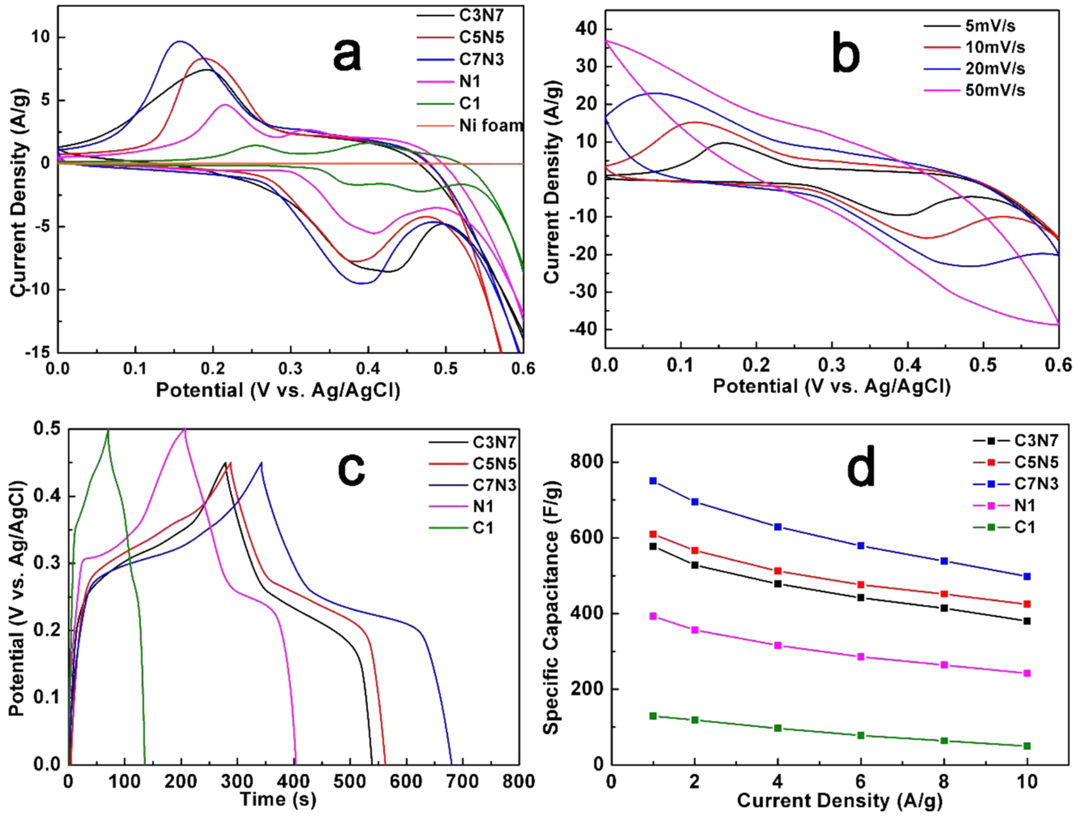

Figure 4. (a) CV curves of metal oxides and nickel foam at a scan rate of 5 mV/s, (b) CV curves of sample C7N3 at different scan rates, (c) galvanostatic charge−discharge curves of the metal oxides at a current density of 1 A/g, and (d) the specific capacitance as a function of current density for the metal oxide samples showing their rate capabilities.

$$\mathrm{NiCo_2O_4 + OH^- + H_2O = NiOOH + 2CoOOH + e^-} \tag{3}$$

$$\mathrm{CoOOH + OH^- = CoO_2 + H_2O + e^-} \tag{4}$$

For Ni−Co binary oxides, only two pairs of redox peaks exist, because the redox potential of Ni^{2+}/Ni^{3+} and Co^{2+}/Co^{3+} transitions is so close that it is difficult to tell them apart. It is noted that Ni−Co binary oxides show lower reduction potential than NiO and Co_3O_4 electrodes, which may be due to its high valence ions, such as Ni^{3+} and Co^{3+}, as proved by XPS results. Moreover, the peak current of the binary oxides is much higher than those under the same scan rate. It is also known that the area surrounded by the CV curve reflects the electrochemical performance of the electrode materials. The higher the response current density, the larger the specific capacitance of the material delivered.[56] It can be concluded that binary oxides exhibit a higher capacity than that of NiO and Co_3O_4. Among these binary metal oxides, sample C7N3 has the highest peak current, signifying the best electrochemical performance. Sample C7N3 has the largest integral area, implying that it possesses the highest specific capacitance. Figure 4b shows the CV curves of sample C7N3 electrode at different scan rates. The separation between cathodic and anodic peaks gradually increases with increasing scan rate, which may be ascribed to decrease in the utilization of active material caused by limited diffusion/migration of ions at the high scan rate.

Galvanostatic charge−discharge measurements were carried out to further study the specific capacitance and the rate capability of Ni−Co oxides electrodes. Figure 4c shows the charge−discharge curves of the transition metal oxides at the current density of 1 A/g. The nearly symmetric potential-time curves imply the high charge−discharge columbic efficiency and low polarization of the Ni−Co oxides. The specific capacitance can be calculated by the following equation:

$$C = I\Delta t/(m\Delta V) \tag{5}$$

where C (F/g) is the specific capacitance of the electrode, I (A) is the discharge current, Δt (s) is the discharge time, m (g) is the mass of active material, and ΔV (V) is the potential window. The specific capacitances are calculated to be 578, 610, 750, 393, and 129 F/g for sample C3N7, C5N5, C7N3, N1, and C1, respectively, at the current density of 1 A/g. It is also clearly indicated that the specific capacitances of Ni−Co binary oxides are much higher than that of monometallic NiO and Co_3O_4 electrodes, well consistent with CV results. This result can be attributed to the synergetic effect of Ni−Co species as well as the highly electroactive $NiCo_2O_4$ in the binary Ni−Co oxide, even though both the specific surface area and pore volume of NiO is the higher than those of binary oxides.

Figure 4d shows the rate capability of transition metal oxides at the current densities from 1 to 10 A/g. It can be found that the specific capacitances of all samples decrease with the increase of current densities. It is commonly due to more difficult penetration and diffusion of the electrolyte under a high current density.[56,57] The calculated specific capacitances are 380, 424, 498, 242, and 50 F/g for sample C3N7, C5N5, C7N3, N1, and C1 at the current density of 10 A/g, respectively. Furthermore, it can be observed that sample C7N3 still has the highest specific capacitance and the fairly good rate capability among them. The reason for this phenomenon is that the electrochemical reactions usually

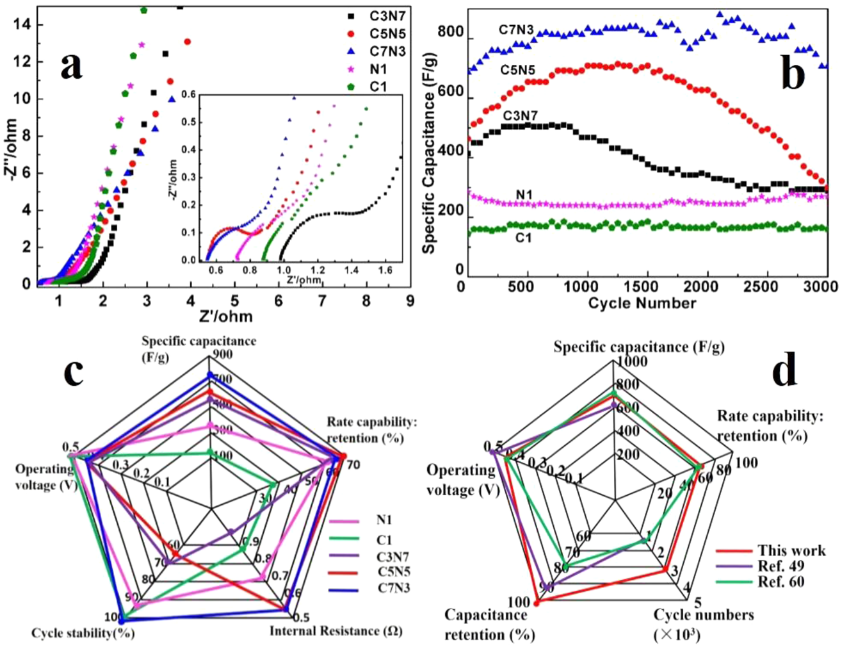

Figure 5. (a) Nyquist impedance plots for all transition metal oxide samples, inset showing the impedance at a high-frequency region; (b) cycling stability of the samples at a current density of 3A/g; (c) example radar plots to compare electrochemical properties of transition metal oxides prepared in this work, (d) with those of in other references.

depend on the insertion−extraction of OH^- from the electrolyte, while the porous structure is beneficial for the ions to diffuse into the electrode holes. In addition, binary oxides, typically for $NiCo_2O_4$, can afford a richer variety of redox reactions (contributed by both Co^{3+} and Ni^{2+} ions) and much higher electrical conductivity than those of the monometallic oxide materials.[58]

EIS tests were measured to evaluate the electrochemical behavior of samples in the frequency range from 0.01 Hz to 10 kHz, as shown in Figure 5a. Each of the plots consists of two sections, a small semicircle at the high-frequency region that can be ascribed to charge transfer resistance and a slope line at the low-frequency region that can be ascribed to mass transfer resistivity of the electrolyte within the pore of the electrode.[59,60] The intercept at the real axis in the high-frequency region represents the internal resistance, including the contact resistance of the interface between active material and current collector, the intrinsic resistance of the active material and the ionic resistance of the electrolyte. In Nyquist plots, all of the samples manifest a small real axis intercept (<1.0 Ω), showing a low internal resistance. It is obvious that sample C7N3 has the lowest internal resistance among them, indicating that it exhibits the highest electrical conductivity.

Cycling stability tests were conducted by means of galvanostatic charge−discharge over 3000 cycles at a current density of 3 A/g. As shown in Figure 5b, samples N1 and C1 exhibit excellent cycling stability (capacitance retention: 94.7% for N1, 100% for C1) but a rather low specific capacitance. This may be ascribed to the high conductivity and reversibility. For binary transition metal oxides, their specific capacitances are significantly high; however, the combination of Ni and Co may lead to a looser structure, resulting in a relatively poor cycling stability of binary oxides compared with C1 and N1. The cycling stability for sample C3N7 and C5N5 is obviously worse than sample C7N3. The specific capacitance of sample C3N7 and C5N5 decreases quickly after 1000 and 1500 cycles, respectively. It should be caused by the low content of $NiCo_2O_4$ in them. Sample C7N3 has a good cycling stability (102% retention after 3000 cycles) with a slight fluctuation and the highest specific capacitance among them, which means that it is an attractive candidate as electrode material for SCs due to its high specific capacitance, good rate capability, and long-term cycling life. It is noteworthy that the specific capacitances of samples C3N7, C5N5, and C7N3 increase at first, instead of decreasing as sample C1 and N1, and then decrease with cycling numbers. This is ascribed to the cycling induced improvement in the surface wetting of the electrode and electrolyte ions accessibility, thus resulting in more electroactive surface area. The following decline can be ascribed to irreversible surface dissolution of unstable materials and solid electrode interface reaction.[61]

An example radar plot to compare electrochemical properties of transition metal oxides prepared in this work with each other is shown in Figure 5c. A larger area encompassed within a radar plot indicates a better overall performance.[62] It can be seen straightforward that sample C7N3 has a much better electrochemical performance than the others. Figure 5d also shows a radar plot to compare electrochemical properties of sample C7N3 prepared in this work (red curve) with those in refs 49 (purple curve) and 60 (green curve). As is apparent from Figure 5d, Ni−Co binary oxide (sample C7N3) in this work exhibits better electrochemical performances than those reported in other references.

In order to find out the reasons for the decline in capacitance during cycling test, the phase of binary oxides electrodes were investigated after 3000 cycling test. The XRD patterns of the binary metal oxide electrodes after 3000 cycling are comparatively shown in Figure 6 in a 2θ angle range from 15° to 42° to avoid the interference of nickel foam substrate. It is clear to see that the XRD patterns of these samples have no other new peaks except for two peaks at 38.4° and 22.7°. The small peak at 22.7° is presented in each pattern, which can be

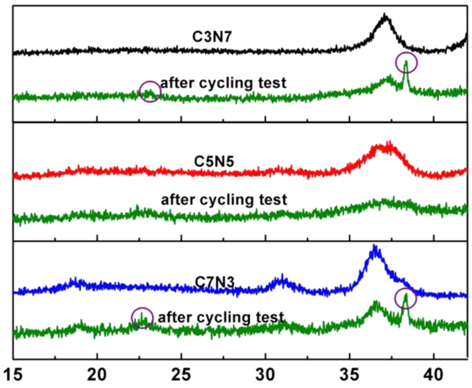

Figure 6. XRD patterns of Ni−Co binary oxide electrodes before and after 3000 cycling test.

ascribed to the presence of polyvinylidene fluoride as a binder.[63] The peak at 38.4° is not presented in every pattern, which can be attributed to the formation of $Ni(OH)_2$ on the nickel foam in alkaline solution. Next step, we try to use another current collector instead of nickel foam to avoid it. However, comparing the XRD patterns before and after the cycling test, we can draw a conclusion that the phase of the binary metal oxides after the cycling test is not changed, showing a good stability in structure.

3.4. Properties of Asymmetric Capacitor. An asymmetric SC with two-electrode configuration was fabricated, since a three-electrode setup could overestimate the performance of the electrode materials. A hybrid capacitor using sample C7N3 as a positive electrode and AC as a negative electrode was assembled. The electrochemical properties of the asymmetric capacitor were evaluated by CV and galvanostatic charge−discharge measurements in a potential window of 0−1.75 V. The mass ratio of sample C7N3 to AC electrode is 1:1.66, as calculated from the results in Figure S7. The total mass of active materials in the asymmetric SC electrodes (1.5 cm × 1.5 cm) is about 13.36 mg here.

The CV curves of the asymmetric capacitor are shown in Figure 7a at the scan rates from 5 to 100 mV/s. It is found that there is no obvious distortion in the CV curves within an operational potential of 1.75 V, indicating its fast charge−discharge properties. Galvanostatic charge−discharge test was carried out at various current densities in order to determine the specific capacitance, energy density, and power density. The charge−discharge curves are illustrated in Figure 7b, which tend toward a triangular-like shape. The calculated specific capacitance based on the total mass loading as a function of current densities is shown in the inset of Figure 7c. The specific capacitance decreased from 82.1 to 46.9 F/g, when the current density increased from 1 to 10 A/g, suggesting a fairly good rate capability of the hybrid capacitor. Figure 7c shows the Ragone plot of the C7N3//AC asymmetric capacitor. The hybrid capacitor can deliver an energy density of 34.9 Wh/kg at 875 W/kg and still remain 19.9 Wh/kg at 8750W/kg. It proves that the hybrid capacitor is capable of delivering a high power density without substantial degradation in the stored energy. We also illustrated the capacitance values of reported literature

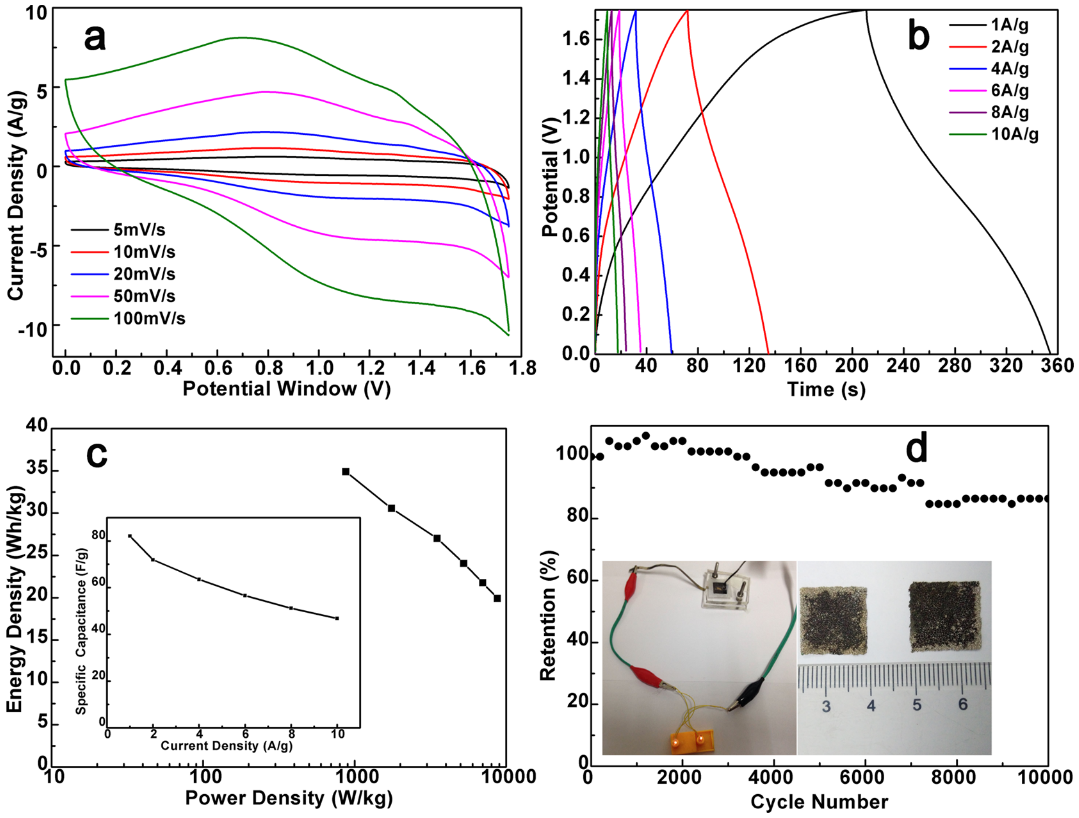

Figure 7. Electrochemical performances of the asymmetric SC using C7N3//AC (a) CV curves at various scan rates, (b) charge−discharge curves under different current densities from 1 to 10 A/g, (c) the corresponding Ragone plot, inset showing the specific capacitance dependent on current densities, and (d) cycling stability at a current density of 2A/g, inset showing the photograph of two lights connected to an asymmetric capacitor and the size of the two electrodes.

Table 3. Specific Capacitance of Transition Metal Oxides as Positive Electrode of Asymmetric Capacitors Reported in Some Papers

sample	specific capacitance (F/g)	voltage (V)	mass loading (mg)	preparation method	ref
Co_3O_4 nanowire	57.4 (1A/g)	1.5	—	hydrothermal	64
NiO@graphene foam	116 (1 A/g)	1.4	—	pulsed laser deposition	65
NiO@carbon	102.38 (1A/g)	1.6	0.71	electrodeposition	66
$NiCo_2O_4$	105 (3.6 mA/cm^2)	1.6	—	hydrothermal	27
$NiCo_2O_4$	49.3 (1A/g)	1.5	—	electrodeposition	49
$NiCo_2O_4$	60 (1A/g)	1.2	—	chemical bath deposition	35
$NiCo_2O_4$	64.7 (1 mA/cm^2)	1.8	—	hydrothermal	30
CNT@NiCo2O4	91 (0.5 A/g)	1.25	—	coprecipitation	67
$Ni_{0.8}Cu_{0.2}Co_2O_4$	72	1.5	—	sol−gel	68
$Ni_{1.46}Mn_{0.36}Co_{1.18}Ox$	86.7 (1A/g)	1.5	1.84 mg/cm^2	hydrothermal	69
$NiCo_2O_4$−NiO	82.1 (1A/g)	1.75	13.36	hydrothermal	this work

in comparison with that of our case, as demonstrated in Table 3. It is obvious that the sample C7N3 ($NiCo_2O_4$−NiO) prepared in this work shows a high specific capacitance with a large potential window.

The cycling stability of the asymmetric SC was also examined in the potential window of 1.75 V at the current density of 2 A/g to evaluate if it was suitable for long-term application. As shown in Figure 7d, the asymmetric SC displays a little degradation, with 86.4% retention of the initial value after 10000 cycles. It indicates a quite excellent cycling stability, making it a promising candidate for energy storage materials. After 10000 cycling test, we used the capacitor to connect two parallel small lamps (driving voltage, 1.5 V). The two lights can work for 12 s, after being charged to 1.75 V at the charge current density of 1 A/g and decrease to 7 s at the charge current density of 10 A/g, which is consistent with the above results. The excellent electrochemical properties are mainly attributed to the high conductivity and capacitance of the capacitor derived from the redox reactions of Ni^{2+}/Ni^{3+} and Co^{2+}/Co^{3+}, which is superior in charge transfer kinetics.[48] In addition, the porous structure of $NiCo_2O_4$ can facilitate ion and electron transfer, restricting the volumetric change of the electrode in the charge−discharge process. This demonstrates that the hybrid capacitor can be efficiently used as a potential power source with excellent stability.

CONCLUSION

In summary, we reported a facile method to prepare porous Ni−Co binary oxides by combining hydrothermal method with following heat treatment. The composition and porous features of the metal oxides could easily be tuned. Varying the Ni/Co ratio allows the formation of 3D porous metal oxides with different specific surface areas and pore volumes under the same annealing temperature. Electrochemical tests demonstrate that the binary metal oxides exhibit better electrochemical properties than monometallic oxide. Among them, sample C7N3 with a high content of $NiCo_2O_4$ has the highest specific capacitance of 750 F/g, high rate capability, and long-term cycling stability (102% retention after 3000 cycles). Therefore, Ni−Co binary oxides are promising electrode materials for SCs. The assembled hybrid asymmetric capacitor using sample C7N3 as the positive electrode and activated carbon as the negative electrode can work in a broad potential window of 1.75 V with a high specific capacitance (82.1 F/g), high energy density (34.9 Wh/kg), and long cycle life (86.4% retention after 10000 cycles), which is encouraging for the application of SC.

ASSOCIATED CONTENT

Supporting Information

The Supporting Information is available free of charge on the ACS Publications website at DOI: 10.1021/acsami.5b04463.

SEM images and EDS spectra of transition metal hydroxides as the precursors of metal oxides, EDS mappings and XPS data of sample C7N3, nitrogen adsorption−desorption isotherms, XRD pattern of polyvinylidene fluoride, and CV curves of AC and binary metal oxide (sample C7N3) (PDF)

AUTHOR INFORMATION

Corresponding Author

*E-mail: chengjp@zju.edu.cn. Tel/Fax: +86-571-87951411.

Notes

The authors declare no competing financial interest.

ACKNOWLEDGMENTS

This work was financially supported by Zhejiang Provincial Natural Science foundation of China (Grant LY13E020002) and Public Projects (analysis and test) of Zhejiang Province (Grant 2015C37027).

REFERENCES

(1) Wang, G. P.; Zhang, L.; Zhang, J. J. A Review of Electrode Materials for Electrochemical Supercapacitors. *Chem. Soc. Rev.* **2012**, *41*, 797−828.

(2) Chen, H.; Hu, L. F.; Yan, Y.; Che, R. C.; Chen, M.; Wu, L. M. One-Step Fabrication of Ultrathin Porous Nickel Hydroxide-Manganese Dioxide Hybrid Nanosheets for Supercapacitor Electrodes with Excellent Capacitive Performance. *Adv. Energy Mater.* **2013**, *3* (12), 1636−1646.

(3) Chen, H.; Zhou, S. X.; Wu, L. M. Porous Nickel Hydroxide-Manganese Dioxide-Reduced Graphene Oxide Ternary Hybrid Spheres as Excellent Supercapacitor Electrode Materials. *ACS Appl. Mater. Interfaces* **2014**, *6* (11), 8621−8630.

(4) Cheng, J. P.; Zhang, J.; Liu, F. Recent Development of Metal Hydroxides as Electrode Material of Electrochemical Capacitors. *RSC Adv.* **2014**, *4*, 38893−38917.

(5) Zhang, W. F.; Liu, F.; Li, Q. Q.; Shou, Q. L.; Cheng, J. P.; Zhang, L.; Nelson, B. J.; Zhang, X. B. Transition Metal Oxide and Graphene Nanocomposites for High-Performance Electrochemical Capacitors. *Phys. Chem. Chem. Phys.* **2012**, *14*, 16331−16337.

(6) Yang, L.; Qian, L.; Tian, X. Q.; Li, J.; Dai, J. Y.; Guo, Y.; Xiao, D. Hierarchically Porous Nickel Oxide Nanosheets Grown on Nickel Foam Prepared by One-Step In Situ Anodization for High-Performance Supercapacitors. *Chem. - Asian J.* **2014**, *9*, 1579−1585.

(7) Feng, L. D.; Zhu, Y. F.; Ding, H. Y.; Ni, C. Y. Recent Progress in Nickel Based Materials for High Performance Pseudocapacitor Electrodes. *J. Power Sources* **2014**, *267*, 430−444.

(8) Liu, J. P.; Jiang, J.; Bosman, M.; Fan, H. J. Three-Dimensional Tubular Arrays of MnO_2−NiO Nanoflakes with High Areal Pseudocapacitance. *J. Mater. Chem.* **2012**, *22*, 2419−2426.

(9) Padmanathan, N.; Selladurai, S. Electrochemical Capacitance of Porous NiO−CeO_2 Binary Oxide Synthesized via Sol−Gel Technique for Supercapacitor. *Ionics* **2014**, *20*, 409−420.

(10) Kim, J. H.; Zhu, K.; Yan, Y. F.; Perkins, C. L.; Frank, A. J. Microstructure and Pseudocapacitive Properties of Electrodes Constructed of Oriented NiO-TiO_2 Nanotube Arrays. *Nano Lett.* **2010**, *10*, 4099−4104.

(11) Liu, M. C.; Kong, L. B.; Lu, C.; Li, X. M.; Luo, Y. C.; Kang, L. A Sol-Gel Process for Fabrication of NiO/$NiCo_2O_4$/Co_3O_4 Composite with Improved Electrochemical Behavior for Electrochemical Capacitors. *ACS Appl. Mater. Interfaces* **2012**, *4*, 4631−4636.

(12) Yang, J.-H.; Yu, Q.; Li, Y.; Mao, L.; Ma, D. Batch Fabrication of Mesoporous Boron-Doped Nickel Oxide Nanoflowers for Electrochemical Capacitors. *Mater. Res. Bull.* **2014**, *59*, 382−386.

(13) Xia, X. H.; Tu, J. P.; Mai, Y. J.; Chen, R.; Wang, X. L.; Gu, C. D.; Zhao, X. B. Graphene Sheet/Porous NiO Hybrid Film for Supercapacitor Applications. *Chem. - Eur. J.* **2011**, *17*, 10898−10905.

(14) Yuan, C. Z.; Wu, H. B.; Xie, Y.; Lou, X. W. Mixed Transition-Metal Oxides: Design, Synthesis, and Energy-Related Applications. *Angew. Chem., Int. Ed.* **2014**, *53*, 1488−1504.

(15) Zhang, Y. J.; Liu, Y. Y.; Chen, J.; Guo, Q. F.; Wang, T.; Pang, H. Cobalt Vanadium Oxide Thin Nanoplates: Primary Electrochemical Capacitor Application. *Sci. Rep.* **2014**, *4*, 5687.

(16) Lee, M.-T.; Chang, J.-K.; Tsai, W.-T.; Lin, C.-K. In Situ X-ray Absorption Spectroscopic Studies of Anodically Deposited Binary Mn−Fe Mixed Oxides with Relevance to Pseudocapacitance. *J. Power Sources* **2008**, *178*, 476−482.

(17) Chang, K.-H.; Hu, C.-C. Hydrothermal Synthesis of Binary Ru−Ti Oxides with Excellent Performances for Supercapacitors. *Electrochim. Acta* **2006**, *52*, 1749−1757.

(18) Gomez, J.; Kalu, E. E.; Nelson, R.; Weatherspoon, M. H.; Zheng, J. P. Binder-Free Co−Mn Composite Oxide for Li−Air Battery Electrode. *J. Mater. Chem. A* **2013**, *1*, 3287−3294.

(19) Chen, Y.-S.; Hu, C.-C. Capacitive Characteristics of Binary Manganese-Nickel Oxides Prepared by Anodic Deposition. *Electrochem. Solid-State Lett.* **2003**, *6*, A210−A213.

(20) Lu, X. H.; Huang, X.; Xie, S. L.; Zhai, T.; Wang, C. S.; Zhang, P.; Yu, M. H.; Li, W.; Liang, C. L.; Tong, Y. X. Controllable Synthesis of Porous Nickel−Cobalt Oxide Nanosheets for Supercapacitors. *J. Mater. Chem.* **2012**, *22*, 13357−13364.

(21) Naveen, A. N.; Selladurai, S. Investigation on Physiochemical Properties of Mn Substituted Spinel Cobalt Oxide for Supercapacitor Applications. *Electrochim. Acta* **2014**, *125*, 404−414.

(22) Wang, Z. X.; Zhu, J. L.; Sun, P.; Zhang, P. Y.; Zeng, Z. F.; Liang, S.; Zhu, X. H. Nanostructured Mn−Cu Binary Oxides for Supercapacitor. *J. Alloys Compd.* **2014**, *598*, 166−170.

(23) Yuan, C. Z.; Hou, L. R.; Li, D. K.; Zhang, Y. W.; Xiong, S. L.; Zhang, X. G. Unusual Electrochemical Behavior of Ru−Cr Binary Oxide-Based Aqueous Symmetric Supercapacitors in KOH Solution. *Electrochim. Acta* **2013**, *88*, 654−658.

(24) Yang, Y.; Kim, D.; Yang, M.; Schmuki, P. Vertically Aligned Mixed V_2O_5-TiO_2 Nanotube Arrays for Supercapacitor Applications. *Chem. Commun.* **2011**, *47*, 7746−7748.

(25) Li, L.; Zhang, Y. Q.; Liu, X. Y.; Shi, S. J.; Zhao, X. Y.; Zhang, H.; Ge, X.; Cai, G. F.; Gu, C. D.; Wang, X. L.; Tu, J. P. One-Dimension $MnCo_2O_4$ Nanowire Arrays for Electrochemical Energy Storage. *Electrochim. Acta* **2014**, *116*, 467−474.

(26) Gong, X. F.; Cheng, J. P.; Liu, F.; Zhang, L.; Zhang, X. B. Nickel−Cobalt Hydroxide Microspheres Electrodepositioned on Nickel Cobaltite Nanowires Grown on Ni Foam for High-Performance Pseudocapacitors. *J. Power Sources* **2014**, *267*, 610−616.

(27) Wang, X.; Yan, C. Y.; Sumboja, A.; Lee, P. S. High Performance Porous Nickel Cobalt Oxide Nanowires for Asymmetric Supercapacitor. *Nano Energy* **2014**, *3*, 119−126.

(28) Zhang, J.; Cheng, J. P.; Li, M.; Liu, L.; Liu, F.; Zhang, X. B. Flower-Like Nickel−Cobalt Binary Hydroxides with High Specific Capacitance: Tuning the Composition and Asymmetric Capacitor Application. *J. Electroanal. Chem.* **2015**, *743*, 38−45.

(29) Patil, U. M.; Sohn, J. S.; Kulkarni, S. B.; Lee, S. C.; Park, H. G.; Gurav, K. V.; Kim, J. H.; Jun, S. C. Enhanced Supercapacitive Performance of Chemically Grown Cobalt-Nickel Hydroxides on Three-Dimensional Graphene Foam Electrodes. *ACS Appl. Mater. Interfaces* **2014**, *6* (4), 2450−2458.

(30) Zhu, J. H.; Jiang, J.; Sun, Z. P.; Luo, J. S.; Fan, Z. X.; Huang, X. T.; Zhang, H.; Yu, T. 3D Carbon/Cobalt-Nickel Mixed-Oxide Hybrid Nanostructured Arrays for Asymmetric Supercapacitors. *Small* **2014**, *10*, 2937−2945.

(31) Xiong, G. P.; Meng, C. Z.; Reifenberger, R. G.; Irazoqui, P. P.; Fisher, T. S. Graphitic Petal Electrodes for All-Solid-State Flexible Supercapacitors. *Adv. Energy Mater.* **2014**, *4* (3), 1300515.

(32) Kurra, N.; Alhebshi, N. A.; Alshareef, H. N. Microfabricated Pseudocapacitors Using $Ni(OH)_2$ Electrodes Exhibit Remarkable Volumetric Capacitance and Energy Density. *Adv. Energy Mater.* **2015**, *5* (2), 1401303.

(33) Xiong, G. P.; Hembram, K. P. S. S.; Reifenberger, R. G.; Fisher, T. S. MnO_2-Coated Graphitic Petals for Supercapacitor Electrodes. *J. Power Sources* **2013**, *227*, 254−259.

(34) Tang, C. H.; Tang, Z.; Gong, H. Hierarchically Porous Ni-Co Oxide for High Reversibility Asymmetric Full-Cell Supercapacitors. *J. Electrochem. Soc.* **2012**, *159*, A651−A656.

(35) Fan, Z.; Chen, J. H.; Cui, K. Z.; Sun, F.; Xu, Y.; Kuang, Y. F. Preparation and Capacitive Properties of Cobalt−Nickel Oxides/Carbon Nanotube Composites. *Electrochim. Acta* **2007**, *52*, 2959−2965.

(36) Lei, Y.; Li, J.; Wang, Y. Y.; Gu, L.; Chang, Y. F.; Yuan, H. Y.; Xiao, D. Rapid Microwave-Assisted Green Synthesis of 3D Hierarchical Flower-Shaped $NiCo_2O_4$ Microsphere for High-Performance Supercapacitor. *ACS Appl. Mater. Interfaces* **2014**, *6* (3), 1773−1780.

(37) Srivastava, M.; Elias Uddin, M.; Singh, J.; Kim, N. H.; Lee, J. H. Preparation and Characterization of Self-Assembled Layer by Layer $NiCo_2O_4$−Reduced Graphene Oxide Nanocomposite with Improved Electrocatalytic Properties. *J. Alloys Compd.* **2014**, *590*, 266−276.

(38) Lian, K.; Kirk, D. W.; Thorpe, S. J. Electrocatalytic Behaviour of Ni-Base Amorphous Alloys. *Electrochim. Acta* **1991**, *36*, 537−545.

(39) Hu, G. X.; Tang, C. H.; Li, C. X.; Li, H. M.; Wang, Y.; Gong, H. The Sol-Gel-Derived Nickel-Cobalt Oxides with High Supercapacitor Performances. *J. Electrochem. Soc.* **2011**, *158*, A695−A699.

(40) Wang, R. T.; Yan, X. B. Superior Asymmetric Supercapacitor Based on Ni-Co Oxide Nanosheets and Carbon Nanorods. *Sci. Rep.* **2014**, *4*, 3712.

(41) Sarma, B.; Ray, R. S.; Mohanty, S. K.; Misra, M. Synergistic Enhancement in the Capacitance of Nickel and Cobalt Based Mixed Oxide Supercapacitor Prepared by Electrodeposition. *Appl. Surf. Sci.* **2014**, *300*, 29−36.

(42) Shen, L. F.; Che, Q.; Li, H. S.; Zhang, X. G. Mesoporous $NiCo_2O_4$ Nanowire Arrays Grown on Carbon Textiles as Binder-Free Flexible Electrodes for Energy Storage. *Adv. Funct. Mater.* **2014**, *24*, 2630−2637.

(43) Wu, H. B.; Pang, H.; Lou, X. W. Facile Synthesis of Mesoporous $Ni_{0.3}Co_{2.7}O_4$ Hierarchical Structures for High-Performance Supercapacitors. *Energy Environ. Sci.* **2013**, *6*, 3619−3626.

(44) Deng, J.-J.; Deng, J.-C.; Liu, Z.-L.; Deng, H.-R.; Liu, B. Influence of Addition of Cobalt Oxide on Microstructure and Electrochemical Capacitive Performance of Nickel Oxide. *J. Solid State Electrochem.* **2009**, *13*, 1387−1394.

(45) Cheng, J. P.; Shou, Q. L.; Wu, J. S.; Liu, F.; Dravid, V. P.; Zhang, X. B. Influence of Component Content on the Capacitance of Magnetite/Reduced Graphene Oxide Composite. *J. Electroanal. Chem.* **2013**, *698*, 1−8.

(46) Cheng, J. P.; Zhang, X. B.; Ye, Y. Reduction Process of Nickel Cations Anchored on Carbon Nanotubes. *J. Mater. Process. Technol.* **2008**, *206*, 180−183.

(47) Marco, J. F.; Gancedo, J. R.; Gracia, M.; Gautier, J. L.; Ríos, E. I.; Palmer, H. M.; Greaves, C.; Berry, F. J. Cation Distribution and Magnetic Structure of the Ferrimagnetic Spinel $NiCo_2O_4$. *J. Mater. Chem.* **2001**, *11*, 3087−3093.

(48) Tang, Q. Q.; Chen, M. M.; Wang, L.; Wang, G. C. A Novel Asymmetric Supercapacitors Based on Binder-Free Carbon Fiber Paper@ Nickel Cobaltite Nanowires and Graphene Foam Electrodes. *J. Power Sources* **2015**, *273*, 654−662.

(49) Lu, X.-F.; Wu, D.-J.; Li, R.-Z.; Li, Q.; Ye, S.-H.; Tong, Y.-X.; Li, G.-R. Hierarchical $NiCo_2O_4$ Nanosheets@Hollow Microrod Arrays for High-Performance Asymmetric Supercapacitors. *J. Mater. Chem. A* **2014**, *2*, 4706−4713.

(50) Verma, S.; Joshi, H. M.; Jagadale, T.; Chawla, A.; Chandra, R.; Ogale, S. Nearly Monodispersed Multifunctional $NiCo_2O_4$ Spinel Nanoparticles: Magnetism, Infrared Transparency, and Radiofrequency Absorption. *J. Phys. Chem. C* **2008**, *112*, 15106−15112.

(51) Hu, L. F.; Wu, L. M.; Liao, M. Y.; Hu, X. H.; Fang, X. S. Electrical Transport Properties of Large, Individual $NiCo_2O_4$ Nanoplates. *Adv. Funct. Mater.* **2012**, *22*, 998−1004.

(52) Wu, Z. B.; Zhu, Y. R.; Ji, X. B. $NiCo_2O_4$-Based Materials for Electrochemical Supercapacitors. *J. Mater. Chem. A* **2014**, *2* (36), 14759−14772.

(53) Dubal, D. P.; Gomez-Romero, P.; Sankapal, B. R.; Holze, R. Nickel Cobaltite as an Emerging Material for Supercapacitors: An Overview. *Nano Energy* **2015**, *11*, 377−399.

(54) Zheng, H. S.; Ni, Y. H.; Wan, F. Y.; Ma, X. Fast Synthesis and Electrochemical Performance of Hollow $NiCo_2O_4$ Flowerlike Microstructures. *RSC Adv.* **2015**, *5* (40), 31558−31565.

(55) Chen, X.; Cheng, J. P.; Shou, Q. L.; Liu, F.; Zhang, X. B. Effect of Calcination Temperature on the Porous Structure of Cobalt Oxide Micro-flowers. *CrystEngComm* **2012**, *14*, 1271−1276.

(56) Li, M.; Cheng, J. P.; Fang, J. H.; Yang, Y.; Liu, F.; Zhang, X. B. NiAl-Layered Double Hydroxide/Reduced Graphene Oxide Composite: Microwave-Assisted Synthesis and Supercapacitive Properties. *Electrochim. Acta* **2014**, *134*, 309−318.

(57) Cheng, J. P.; Fang, J. H.; Li, M.; Zhang, W. F.; Liu, F.; Zhang, X. B. Enhanced Electrochemical Performance of CoAl-Layered Double Hydroxide Nanosheet Arrays Coated by Platinum Films. *Electrochim. Acta* **2013**, *114*, 68−75.

(58) Zhang, Y. F.; Ma, M. Z.; Yang, J.; Su, H. Q.; Huang, W.; Dong, X. C. Selective Synthesis of Hierarchical Mesoporous Spinel $NiCo_2O_4$ for High-Performance Supercapacitors. *Nanoscale* **2014**, *6*, 4303−4308.

(59) Xu, J. M.; Wu, J. S.; Luo, L. L.; Chen, X. Q.; Qin, H. B.; Dravid, V.; Mi, S. B.; Jia, C. L. Co_3O_4 Nanocubes Homogeneously Assembled on Few-Layer Graphene for High Energy Density Lithium-Ion Batteries. *J. Power Sources* **2015**, *274*, 816−822.

(60) Jokar, E.; Iraji zad, A.; Shahrokhian, S. Synthesis and Characterization of $NiCo_2O_4$ Nanorods for Preparation of Supercapacitor Electrodes. *J. Solid State Electrochem.* **2015**, *19*, 269−274.

(61) Jiang, W. C.; Yu, D. S.; Zhang, Q.; Goh, K.; Wei, L.; Yong, Y. L.; Jiang, R. R.; Wei, J.; Chen, Y. Ternary Hybrids of Amorphous Nickel Hydroxide-Carbon Nanotube -Conducting Polymer for Supercapacitors with High Energy Density, Excellent Rate Capability, and Long Cycle Life. *Adv. Funct. Mater.* **2015**, *25*, 1063−1073.

(62) Xiong, G. P.; Meng, C. Z.; Reifenberger, R. G.; Irazoqui, P. P.; Fisher, T. S. A Review of Graphene-Based Electrochemical Microsupercapacitors. *Electroanalysis* **2014**, *26*, 30−51.

(63) Cheng, J. P.; Liu, L.; Zhang, J.; Liu, F.; Zhang, X. B. Influences of Anion Exchange and Phase Transformation on the Supercapacitive Properties of α-$Co(OH)_2$. *J. Electroanal. Chem.* **2014**, *722−723*, 23−31.

(64) Liu, W. W.; Li, X.; Zhu, M. H.; He, X. High-Performance All-Solid State Asymmetric Supercapacitor Based on Co_3O_4 Nanowires and Carbon Aerogel. *J. Power Sources* **2015**, *282*, 179−186.

(65) Wang, H. W.; Yi, H.; Chen, X.; Wang, X. F. Asymmetric Supercapacitors Based on Nano-Architectured Nickel Oxide_Graphene Foam and Hierarchical Porous Nitrogen-Doped Carbon Nanotubes with Ultrahigh-Rate Performance. *J. Mater. Chem. A* **2014**, *2*, 3223−3230.

(66) Lu, X.-F.; Lin, J.; Huang, Z.-X.; Li, G.-R. Three-Dimensional Nickel Oxide@Carbon Hollow Hybrid Networks with Enhanced Performance for Electrochemical Energy Storage. *Electrochim. Acta* **2015**, *161*, 236−244.

(67) Cai, F.; Kang, Y. R.; Chen, H. Y.; Chen, M. H.; Li, Q. W. Hierarchical CNT@$NiCo_2O_4$ Core−Shell Hybrid Nanostructure for High-Performance Supercapacitors. *J. Mater. Chem. A* **2014**, *2*, 11509−11515.

(68) Michael, M. S. Role of Cu Substitution on the Pseudocapacitive Performance of Nano-platelet Shaped Spinels, $Ni_xCu_zCo_yO_4$ {x = 1-z, y = 2-z, z = 0.2}. *Electrochim. Acta* **2014**, *120*, 350−358.

(69) Li, L.; Zhang, Y. Q.; Shi, F.; Zhang, Y. J.; Zhang, J. H.; Gu, C. D.; Wang, X. L.; Tu, J. P. Spinel Manganese- Nickel-Cobalt Ternary Oxide Nanowire Array for High-Performance Electrochemical Capacitor Applications. *ACS Appl. Mater. Interfaces* **2014**, *6*, 18040−18047.